Ultrahigh Responsivity of Ternary Sb–Bi–Se Nanowire Photodetectors

Rong Huang, Jie Zhang, Fenfen Wei, Lin Shi, Tao Kong, and Guosheng Cheng**

High-quality single-crystalline ternary $(Sb_{1-x}Bi_x)_2Se_3$ nanowires (NWs) (x = 0–0.88) are synthesized by chemical vapor deposition. Nanowires with x from 0 to 0.75 are indexed as an orthorhombic structure. With increasing Bi incorporation ratio, $(Sb_{1-x}Bi_x)_2Se_3$ NWs exhibit remarkable photoresponsivities, which originate from growing surface Se vacancies and augmented oxygen chemisorptions. Notably, spectra responsivity and external quantum efficiency of an $(Sb_{0.44}Bi_{0.56})_2Se_3$ NW photodetector reach as high as ≈8261.4 A/W and $\approx 1.6 \times 10^6$ %, respectively. Those excellent performances unambiguously demonstrate that Sb–Bi–Se NWs are promising for the utilizations of high-sensitivity and high-speed photodetectors and photoelectronic switches.

1. Introduction

Photoconductivity in a specific semiconductor results from enhanced electrical conductivity induced by photogenerated carriers under light illuminations.[1] With large surface-to-volume ratios and Debye length comparable to their small sizes, one-dimensional (1D) semiconductors, such as nanowires (NWs) and nanoribbons, have exhibited high sensitivity to an incident light.[2,3] By means of doping,[4,5] energy band engineering,[6,7] and nanowire networking,[8] performances of 1D semiconductors-based photodetectors can be further improved. For example, cut-off wavelengths for composition-graded CdS_xSe_{1-x} (x = 0–1) NW photodetectors with regulated band gaps were reported to cover a significant portion of the visible spectrum.[7] In addition, S-doped In_2Se_3 NWs displayed much higher spectra responsivity ($R\lambda$) and external quantum efficiency (EQE) than the undoped In_2Se_3 NWs.[4]

High density of trap states due to dangling bonds at surfaces of 1D semiconductors were believed to improve the photoconductivity.[2] Nowadays, surface roughness and surface chemistry techniques have been utilized to engineer the trap states to optimize the photoconductive gain.[9,10] Unfortunately, poor controllabilities of chemical modifications and surface roughness resulted in a relatively low enhancement of photoconductivity. By incorporating additional atoms into binary compounds, resulting intrinsic defects regulate their optical, electrical or photoelectric properties.[11,12] Taking $Bi_{2-x}In_xSe_3$ for instance,[11] the incorporated In atoms in Bi_2Se_3 lattice leaded into a decreased optical relaxation time and high frequency dielectric constant, as well as free electron concentrations modification through induced substitution-related lattice point defects. Moreover, Surface intrinsic defects are also considerably linked with the composition of 1D ternary compounds. Hence, it will be appreciated to govern the photoelectric performances of 1D ternary semiconductor through surface intrinsic defects modulated by the compositions.

Antimony selenide (Sb_2Se_3) NWs, with a good chemical stability and ≈1.21 eV band gap,[13] have been explored as red light photodetectors.[14,15] However, with low electrical conductivity (dark current ≈ 4 pA under 5 V bias voltage), binary Sb_2Se_3 NW exhibited low $R\lambda$ and EQE,[15] which limited their applications on high-sensitivity photodetection. In this paper, ternary $(Sb_{1-x}Bi_x)_2Se_3$ NWs with various compositions were fabricated in a controllable manner. Logarithmical growth of electrical conductivity and photoconductivity of NW-based photodetectors against increased Bi ratio x were observed under red light illumination. A model of increased surface Se vacancies and augmented oxygen chemisorption was proposed.

2. Results and Discussion

The composition of produced low-dimensional inorganic materials can be regulated by the chemical vapor deposition growth parameters, such as the source materials and the growth temperature. In this work, ternary $(Sb_{1-x}Bi_x)_2Se_3$ NWs with Bi ratio x ranging from 0 to 0.88 were fabricated. The morphologies and elemental analysis of $(Sb_{1-x}Bi_x)_2Se_3$ NWs were first investigated by field-emission scanning electron microscopy (SEM) and X-ray energy dispersive spectroscopy (EDX). As shown in **Figure 1**a, the NWs were in diameters of 70 nm to 250 nm with lengths up to several micrometers. EDX equipped on SEM was used to quantify the components of NWs fabricated under different growth conditions. The x values in $(Sb_{1-x}Bi_x)_2Se_3$ NWs were tuned both by the Bi_2Se_3 ratio in source powders (defined as BS_{ratio}) and the source temperature, as demonstrated in

R. Huang, J. Zhang, F. Wei, Dr. L. Shi, Dr. T. Kong, Prof. G. Cheng
Suzhou Institute of Nano-Tech and Nano-Bionics
Chinese Academy of Sciences
398 Ruoshui Road, Suzhou Industrial Park
Jiangsu 215123, China
E-mail: tkong2009@sinano.ac.cn; gscheng2006@sinano.ac.cn
R. Huang, J. Zhang, F. Wei
University of Chinese Academy of Sciences
19A Yuquan Road, Beijing 100049, China

DOI: 10.1002/adfm.201304176

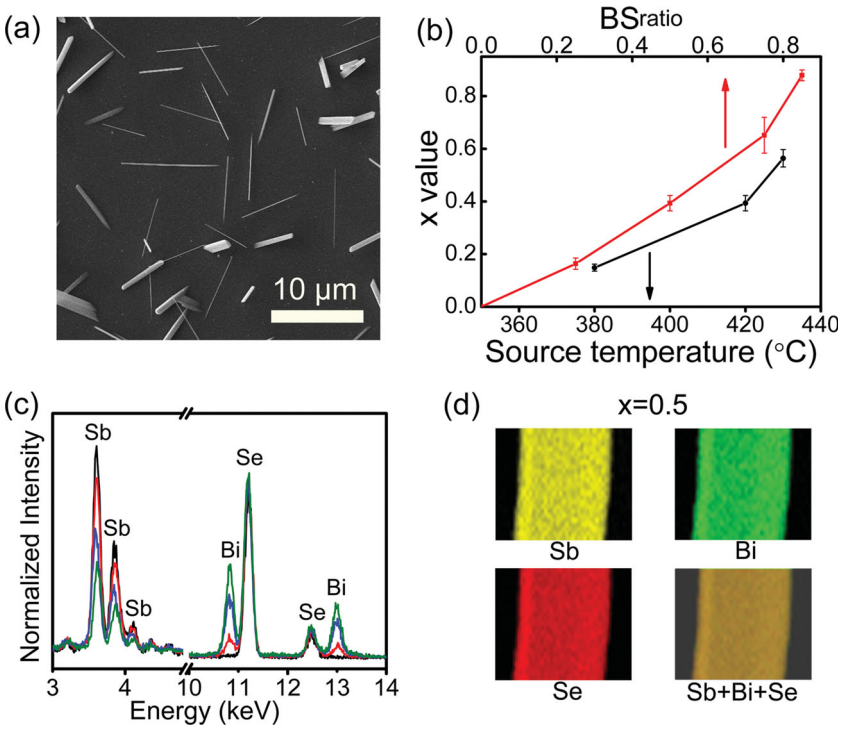

Figure 1. Morphology and composition analysis of obtained Sb–Bi–Se NWs. a) Representative SEM images of fabricated $(Sb_{1-x}Bi_x)_2Se_3$ NWs ($x = 0.56$). b) The composition tuning of ternary $(Sb_{1-x}Bi_x)_2Se_3$ NWs by modifying the BS_{ratio} under 420 °C source temperature (square dot, red line) and by changing the source temperature at $BS_{ratio} = 0.50$ (circle dot, black line), each point denotes an average of twelve NWs data. c) Normalized EDX spectra of different NWs (black, $x = 0$; red, $x = 0.20$; blue, $x = 0.50$; green, $x = 0.75$). d) Elemental mapping of Sb, Bi, and Se by scanning EDX of a $(Sb_{1-x}Bi_x)_2Se_3$ NW ($x = 0.50$).

Figure 1b. Under the same source temperature of 420 °C, Bi content in NWs was raised with increased BS_{ratio} in source powders. On the other hand, x values in NWs magnified from 0.15 to 0.56 when the source temperature increased from 380 °C to 430 °C with $BS_{ratio} = 0.5$, which offered an another way to obtain $(Sb_{1-x}Bi_x)_2Se_3$ NWs spanning a wide range of components. Sb atoms substituted by Bi atoms were deduced from the normalized EDX curves of different NWs in Figure 1c, where Sb peaks shrank as the Bi content increased. Additionally, as observed in Figure 1d, the elemental mapping of Sb, Bi, and Se acquired via scanning EDX of a typical $(Sb_{1-x}Bi_x)_2Se_3$ NW ($x = 0.50$) exhibited homogenous appearance in color, indicating that those elements were uniformly distributed throughout the NW.

To reveal the microstructures of the fabricated $(Sb_{1-x}Bi_x)_2Se_3$ NWs, selected area electron diffraction (SAED) and X-ray diffraction (XRD) were performed. Identical orthorhombic crystal structures with the same growth direction [001] were depicted for $(Sb_{1-x}Bi_x)_2Se_3$ NWs with x ranging from 0 to 0.75 despite a large variation of Bi concentrations, from the SAED patterns and the corresponding micrographs collected by transmission electron microscopy (TEM) (**Figure 2**a). Furthermore, X-ray diffraction (XRD) patterns of $(Sb_{1-x}Bi_x)_2Se_3$ NWs with x from 0.20 to 0.85, together with XRD peaks of Sb_2Se_3 (PCPDF Card No.: 15–0861) and Bi_2Se_3 (PCPDF Card No.: 33–0214) were plotted in Figure 2b. The XRD patterns for $(Sb_{1-x}Bi_x)_2Se_3$ NWs with x below 0.75 were similar with the binary Sb_2Se_3 orthorhombic structure (space group *Pbnm*) despite large difference between Sb and Bi atomic radii (1.45 and 1.60 Å,[16] respectively). However, according to the enlarged XRD spectra shown in Figure S1 (Supporting Information), slight shifts of (020), (120), and (130) peaks to lower diffraction angles were observed, indicating slight lattice constant changes after incorporation of Bi atoms, which was consistent with the small lattice constants difference between orthorhombic Bi_2Se_3 and Sb_2Se_3.[17] On the other hand, orthorhombic and rhombohedral structures ($R\bar{3}m$ space group) coexisted for NWs with $x \approx 0.75$ and mere rhombohedral structure for $x \approx 0.85$ were noticed, indicating a transformation of crystal structure within a composition close to Bi_2Se_3.

Due to a small band gap, Sb_2Se_3 has been integrated in the manufacturing of red light photodetectors. However, acquired low R_λ and EQE were inadequate for high-sensitive photodetection applications. In this work, we aimed at promoting the photodetection performances of semiconducting V-VI selenide nanomaterials by regulation of chemical compositions. Two-electrode devices based on individual $(Sb_{1-x}Bi_x)_2Se_3$-NW for photodetection were defined on Si wafers (with 300 nm SiO_2 layer) using a standard microfabrication process, as schematically illustrated in **Figure 3**a. The $(Sb_{1-x}Bi_x)_2Se_3$ NWs were first dispersed in ethanol solution by ultrasonic processes. Subsequently, the suspension solution was dropped on a Si wafer pre-constructed with external gold electrodes by standard ultraviolet lithography. The bonding pads were then fabricated by electron-beam lithography, followed by magnetron sputtering of titanium/gold (10 nm/100 nm) bilayer deposition and lift-off process. The typical SEM image of $(Sb_{1-x}Bi_x)_2Se_3$ NW nanodevices was present in the inset of Figure 3b. To minimize the effect of NW sizes on photoconduction measurement, NWs with a diameter of ≈100 nm were chosen for nanodevices fabrication and channel length between the two electrodes was designed to be 2 μm.

Photoconductivity of the ternary $(Sb_{1-x}Bi_x)_2Se_3$ NW devices was measured on Agilent B1500A system at room temperature. The current-voltage (I–V) and time-dependent current response (I–t) curves of each single NW device with different x values (0.15, 0.30, 0.45, 0.50, and 0.60) under dark condition and 639 nm light illumination (49.33 mW cm^{-2}) were acquired. Figure 3b presented a typical I–V curves of $(Sb_{1-x}Bi_x)_2Se_3$ NW device at $x = 0.50$. The current across the nanowire was dramatically enhanced under light illumination, compared with that under dark condition. Several cycles of "on" (with incident light) and "off" states (dark condition) were depicted in I–t curve (Figure 3c) of the corresponding NW device, revealing the device had a good photocurrent reversibility and stability. From the magnified current response (Figure 3d), a rise time

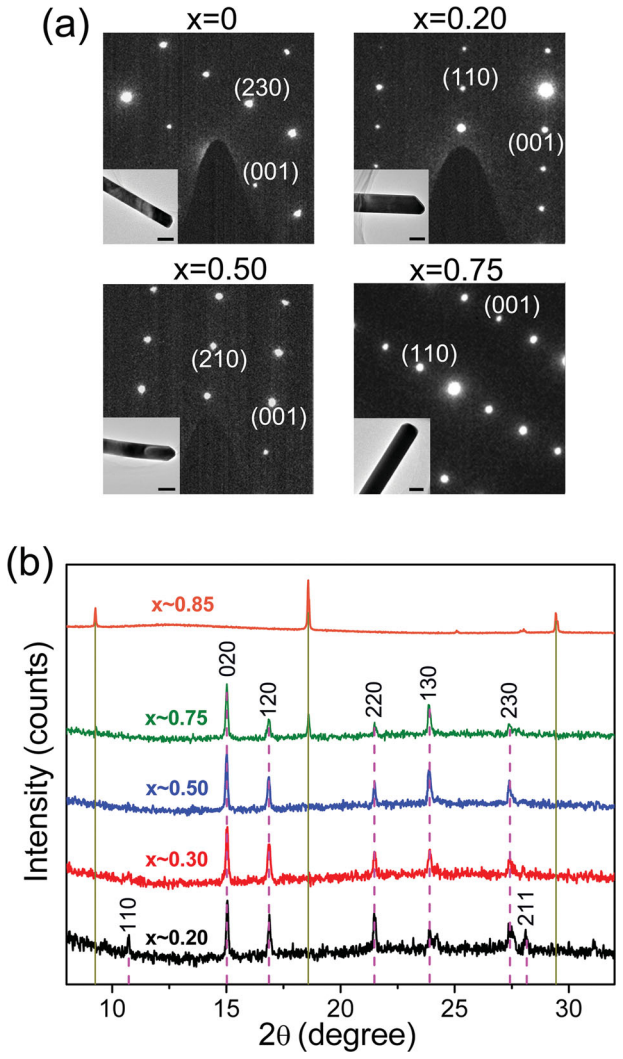

Figure 2. Microstructure characterizations of obtained Sb–Bi–Se NWs. a) SAED patterns of $(Sb_{1-x}Bi_x)_2Se_3$ NWs with variable compositions and the corresponding TEM graphs with the scale bars of 200 nm (insets). b) XRD patterns of $(Sb_{1-x}Bi_x)_2Se_3$ NWs with different Bi ratio x, purple dashed lines and olive solid lines represent for the XRD peaks of Sb_2Se_3 and rhombohedral Bi_2Se_3, respectively.

(RT) < 0.5 s and a decay time (DT) < 0.3 s were extracted. Additionally, I–V and I–t curves for $(Sb_{1-x}Bi_x)_2Se_3$ NWs with other x values were summarized in Figure S2 (Supporting Information), where similar phenomena were observed.

Spectra responsivity (R_λ) (defined as the photocurrent generated per unit power of incident light on the effective area of photoconductor), external quantum efficiency (EQE) (defined as the number of electrons detected per incident photon), and the response time (RT and DT) are commonly used to evaluated the performance of photodetectors.[18] The R_λ and EQE can be expressed as $R_\lambda = I_\lambda (P_\lambda S)^{-1}$ and EQE = $hc R_\lambda (e \lambda)^{-1}$, where I_λ is the photocurrent equaling to illuminated current (I_{light}) minus dark current (I_{dark}), P_λ is the light intensity, S is the effective illuminated area, h is the Planck's constant, c is the velocity of light, e is the electronic charge, and λ is the incident light wavelength.[19] Large values of R_λ and EQE correspond to high sensitivity to incident light for a photodetector. The critical parameters for $(Sb_{1-x}Bi_x)_2Se_3$ NW photoconductors with various compositions were listed in **Table 1**. Calculated $R\lambda$ and EQE of the $(Sb_{1-x}Bi_x)_2Se_3$ NW device with low Bi content ($x = 0.15$) were ≈0.2 A W^{-1} and ≈31%, respectively, which was comparable with those of several 1D semiconductor photodetectors (e.g.,[20] $R_\lambda \approx$ 0.12 A W^{-1} for ZnSe nanoribbons). R_λ as well as EQE apparently elevated by increasing x values was tabulated. Moreover, under light illumination, the current across these NW devices increased by nearly ten times or even dozens of times compared with that under dark conditions, as seen from Table 1. Besides, RT and DT of these NW devices were less than 0.5 s and 0.3 s, respectively, which implied that the NW photodetectors response was much faster compared with other structured photodetectors.[21] It was noteworthy that a $(Sb_{0.44}Bi_{0.56})_2Se_3$ NW device ($x = 0.56$) with a broader and shorter conducting channel for photogenerated carriers (diameter ≈ 122 nm, channel length ≈ 0.88 μm) even possessed much higher photoelectronic sensitivity. According to I–V curves (Figure S3a, Supporting Information) of this NW device, the dark and illuminated currents were as high as 22.209 nA and 459.738 nA, respectively, resulting in ultrahigh R_λ of ≈8261.4 A W^{-1} and EQE of ≈ 1.6×10^6 %. It was nearly 1000-times larger than that of the reported Sb_2Se_3 NW photodetector ($R_\lambda \approx$ 8.0 A W^{-1}, EQE ≈ 1650%),[15] and even much better than the best results from WS_2 nanotube-based red light photodetectors (633 nm, $R_\lambda \approx$ 2360 A W^{-1}).[22] It was found that when x reached about 0.75, the NWs presented no photoelectronic response with resistances as high as ~10^4 Ω. It's probably due to the change of NWs structures to be rhombohedral with high Bi incorporation, resulting the NWs behave more like Bi_2Se_3 with narrow band gap and high carrier density,[23] and perform weak metallic.

It was noted that the dark current, the R_λ, as well as the EQE were all in a nearly logarithmic relationship with x value, as seen in **Figure 4**a and Figure S4 (Supporting Information) which implied incorporated Bi atoms significantly affected on electrical conductivity and photoresponsivity. The incorporation of Bi in $(Sb_{1-x}Bi_x)_2Se_3$ NWs referred to the substitution mechanism where Sb atoms were replaced by larger isovalent Bi atoms, which may result in elevated dark current by modifying the lattice intrinsic defects. In addition, drain-source current (I_{ds}) grown with increasing gate voltage (V_g) in $(Sb_{1-x}Bi_x)_2Se_3$ NW with x = 0.50 was shown in Figure 4b, presenting n-type semiconducting properties, where n-type carriers were probably originated from Se vacancies. Those vacancies were reported as the main source of negatively charged carriers in $Bi_{2-x}Sb_xTe_{3-y}Se_y$ solid solution.[24] To verify the existence of Se vacancies, we calculated the formation energy of Se vacancies [named as $\Delta E(V_{Se})$] both in bulks and on surfaces of Sb_2Se_3 and $SbBiSe_3$ (detailed calculations see the supporting information). The (010) surfaces, identified as the most presented surfaces,[13,25] were further considered for the calculation of formation energy of surface Se vacancies. The lowest $\Delta E(V_{Se})$ for Sb_2Se_3 and $SbBiSe_3$ were calculated as small as 1.383 eV and 1.312 eV in bulk, while 1.337 eV and 1.275 eV on surface, respectively, implying a tendency of Se vacancies formation. Moreover, a smaller $\Delta E(V_{Se})$ of $SbBiSe_3$ proved that the incorporated Bi atoms in $(Sb_{1-x}Bi_x)_2Se_3$ NW would further promote the formation of Se vacancies both in bulks and on surfaces, which

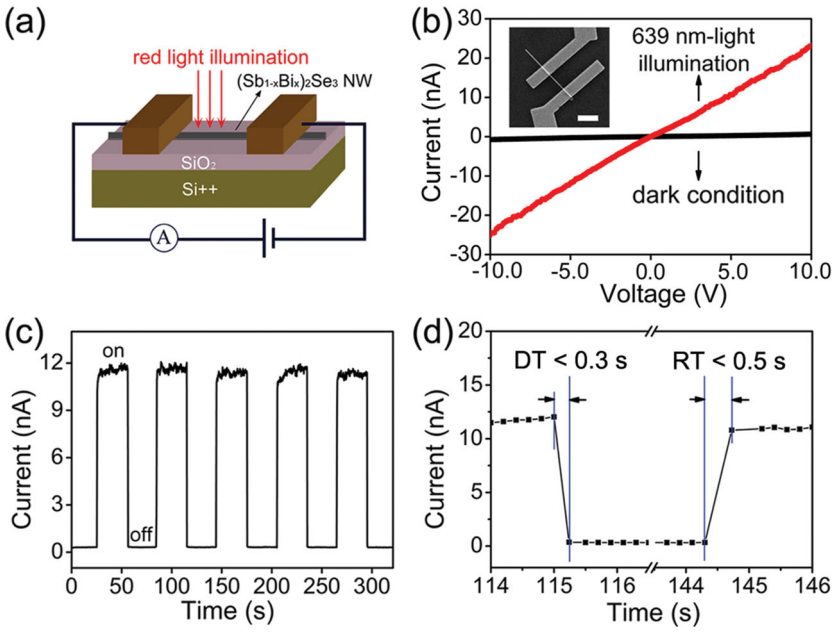

Figure 3. Typical photodetection measurements of $(Sb_{1-x}Bi_x)_2Se_3$ NWs with $x = 0.50$. a) Schematic view of $(Sb_{1-x}Bi_x)_2Se_3$ NW-based two-electrode configuration. b) *I–V* curve of single NW in dark condition and under 639 nm-light illumination (49.33 mW cm^{-2}), respectively. Inset is a SEM image of the NW device with scale bar of 2 μm. c) *I–t* curve of the corresponding NW device to the 639 nm incident light with a period of ≈60 s at an applied voltage of 5 V. d) Magnified current response to scrutinize the rise/decay time.

resulted in an accumulation of free carriers for the increase of dark current.

Surface defects, such as vacancies and dangling bonds, due to high specific surface of nanostructured materials, significantly associate with the high sensitivity of the NWs' photodetection. For example, the metal oxide nanostructures performed an enhanced photosensitivity by introducing abundant surface trap states.[9] Van der Waals interaction breaking of ideal surfaces (010) may result in absence of dangling bonds, while defective surfaces may function the opposite. It was noticed that $\Delta E(V_{Se})$ at surfaces was lower than that in bulks, indicating that Se vacancies formed more easily on surfaces than in bulks for both Sb_2Se_3 and $SbBiSe_3$ configurations. Therefore, accumulation of surface Se vacancies was derived in the $(Sb_{1-x}Bi_x)_2Se_3$ NWs with increased Bi ratio, which resulted in high density of NW surface dangling bonds to promote the photoconduction.

Based on the preceding measurements and calculations, hole-trapping mechanism was proposed to dominate the photoconduction in the $(Sb_{1-x}Bi_x)_2Se_3$ NWs. In this mechanism,[26] under dark condition, oxygen molecules chemisorbed on surface dangling bonds capture the free electrons in n-type semiconductors, which lead to a low-conductivity depletion layer near the surfaces. On the other hand, under illumination, the photogenerated-holes are readily migrate to the surfaces and trapped by the negatively charged oxygen molecules, leaving behind unpaired electrons to increase the conductivity. In this work, the atomic oxygen adsorbed on ideal Sb_2Se_3 (010), $SbBiSe_3$ (010), and Se vacancy defective surfaces was then studied to characterize the oxygen adsorption behavior. Their oxygen adsorption energies were calculated as −0.615 eV, −0.947 eV, −3.445 eV, and −3.608 eV, respectively. Here, the negative values represent for releasing energy in the adsorption process, and the larger absolute values feature more favorable adsorption. According to relaxed surface structures in **Figure 5**, the atomic oxygen chemisorbed on the dangling bonds of surface Sb atoms or Bi atoms. It was deduced that the incorporation of Bi atoms enhanced the atomic oxygen adsorption, along with the formation of surface Se vacancies. Moreover, the oxygen atom chemisorptions are facilitated on the Se-vacancies-contained surfaces than on ideal plain surfaces. Consequently, the substitution-induced surface Se vacancies with augmented oxygen chemisorptions abilities were responsible for the enhanced photoconductivity and responsivity of $(Sb_{1-x}Bi_x)_2Se_3$ NW photodetectors with increased Bi ratio based on a hole-trapping mechanism.

3. Conclusion

In summary, single-crystalline ternary $(Sb_{1-x}Bi_x)_2Se_3$ NWs with x ranging from 0 to 0.88 were synthesized by tuning the source mass ratio and adjusting the source temperature. $(Sb_{1-x}Bi_x)_2Se_3$ NWs with x values below 0.75 of an orthorhombic crystal

Table 1. Critical parameters for $(Sb_{1-x}Bi_x)_2Se_3$ NW photodetectors measured under dark condition and light illumination (639 nm, 49.33 mW cm^{-2}), respectively, at an applied voltage of 5 V with different x values.

x	I_{dark} [nA]	I_λ [nA]	R_λ [A W^{-1}]	EQE [%]	I_{light}/I_{dark}	RT [s]	DT [s]
0.15	0.002	0.016	0.2	31	9	0.47	0.26
0.30	0.023	0.494	4.7	911	22	0.40	0.27
0.45	0.137	5.442	54.9	10674	41	0.42	0.23
0.50	0.276	11.793	118.4	23014	44	0.43	0.24
0.60	2.884	81.886	814.4	158270	29	0.47	0.23

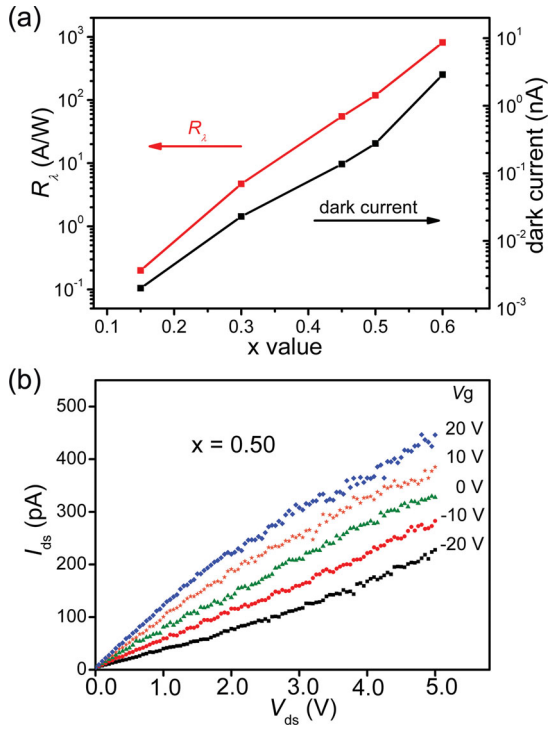

Figure 4. a) The spectra responsivities and the dark currents of $(Sb_{1-x}Bi_x)_2Se_3$ NW devices with varied x under 639 nm light illumination, at 5 V bias voltage. b) Back-gate controlled I_{ds}–V_{ds} curves of a single $(Sb_{0.5}Bi_{0.5})_2Se_3$ NW at room temperature.

structure exhibited photodetection capabilities to 639 nm light. The photoresponsivity of those NWs were dramatically enhanced by growing incorporation of Bi atoms, which were interpreted by the consequentially increased surface Se vacancies and augmented oxygen chemisorption abilities. The models were further verified by theoretical calculations. The excellent photoelectronic performances indicate Bi-rich $(Sb_{1-x}Bi_x)_2Se_3$-NW are one of promising candidates for high-sensitivity and high-speed red light photodetectors.

4. Experimental Section

High-quality single-crystalline ternary $(Sb_{1-x}Bi_x)_2Se_3$ NWs were synthesized by a chemical vapor deposition process which performed in 1-inch-diameter quartz tube mounted in a commercial tube furnace (Thermcraft). A uniform mixture of Sb_2Se_3 and Bi_2Se_3 powder (both 99.999%, from Alfa Aesar) with specific mass ratio was loaded in the central region of the tube as a source materials, while Si wafers decorated with 20 nm Au nanoparticles (Sigma Aldrich) were placed downstream as substrates. The set-up system was then sealed and initially pumped down to a pressure less than 10 mTorr, followed by flushing with high-purity argon for several times to exhaust residual oxygen. High-purity argon of 200 sccm as a carrier gas was injected continually to the tube which maintained a pressure of 10 Torr by using a pumping system before a growth. After that, the source materials were heated to a temperature of 380–430 °C and kept 12 h for a growth of $(Sb_{1-x}Bi_x)_2Se_3$ NWs.

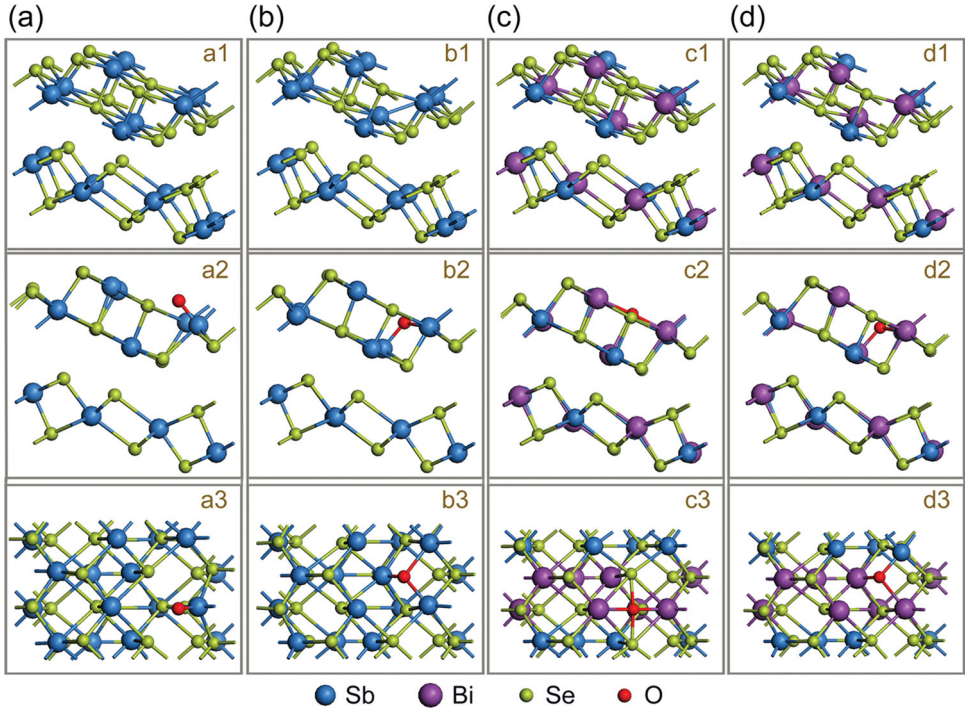

Figure 5. a) Ideal Sb_2Se_3 (010) surface (a1), side view (a2), and top view (a3) of an oxygen adsorbed on ideal Sb_2Se_3 (010) surface. b) Relaxed Sb_2Se_3 (010) surface with a Se vacancy (b1), side view (b2), and top view (b3) of an oxygen adsorbed on Sb_2Se_3 (010) surface with a Se vacancy. c) Ideal $SbBiSe_3$ (010) surface (c1), side view (c2), and top view (c3) of an oxygen adsorbed on ideal $SbBiSe_3$ (010) surface. d) Relaxed $SbBiSe_3$ (010) surface with a Se vacancy (d1), side view (d2), and top view (d3) of an oxygen adsorbed on $SbBiSe_3$ (010) surface with a Se vacancy.

Supporting Information

Supporting Information is available from the Wiley Online Library or from the author.

Acknowledgements

This work was partially funded by the International Science and Technology Corporation Program from the Ministry of Science and Technology of China (MOST) under award number 2010DFB53890, National Natural Science Foundation of China (Grant numbers: 11104317 and 10834004) and Suzhou Science and Technology Program (SYG201332). The authors are grateful for the professional services offered by the Platforms of Characterization & Test and Nanofabrication Facility at Suzhou Institute of Nano-Tech and Nano-Bionics, and Supercomputing Center, CNIC, Chinese Academy of Sciences.

Received: December 15, 2013
Revised: January 18, 2014
Published online: February 26, 2014

[1] T. Y. Zhai, L. Li, Y. Ma, M. Y. Liao, X. Wang, X. S. Fang, J. N. Yao, Y. Bando, D. Golberg, *Chem. Soc. Rev.* **2011**, *40*, 2986.
[2] T. Zhai, L. Li, X. Wang, X. S. Fang, Y. Bando, D. Golberg, *Adv. Funct. Mater.* **2010**, *20*, 4233.
[3] a) L. Peng, L. F. Hu, X. S. Fang, *Adv. Mater.* **2013**, *25*, 5321; b) S. C. Kung, W. D. Xing, W. E. van der Veer, F. Yang, K. C. Donavan, M. Cheng, J. C. Hemminger, R. M. Penner, *ACS Nano* **2011**, *5*, 7627; c) Z. Wang, J. S. Jie, F. Z. Li, L. Wang, T. X. Yan, L. B. Luo, B. A. Nie, C. Xie, P. Jiang, X. W. Zhang, Y. Q. Yu, C. Y. Wu, *ChemPlusChem* **2012**, *77*, 470; d) X. S. Fang, L. F. Hu, K. F. Huo, B. Gao, L. J. Zhao, M. Y. Liao, P. K. Chu, Y. Bando, D. Golberg, *Adv. Funct. Mater.* **2011**, *21*, 3907.
[4] T. Y. Zhai, Y. Ma, L. Li, X. S. Fang, M. Y. Liao, Y. Koide, J. N. Yao, Y. Bando, D. Golberg, *J. Mater. Chem.* **2010**, *20*, 6630.
[5] W. J. Chen, J. K. Wu, J. C. Lin, S. T. Lo, H. D. Lin, D. R. Hang, M. F. Shih, C. T. Liang, Y. H. Chang, *Nanoscale Res. Lett.* **2013**, *8*, 313.
[6] C. Y. Yan, P. S. Lee, *Sci. Adv. Mater.* **2012**, *4*, 241.
[7] T. Takahashi, P. Nichols, K. Takei, A. C. Ford, A. Jamshidi, M. C. Wu, C. Z. Ning, A. Javey, *Nanotechnology* **2012**, *23*, 045201.
[8] a) B. Aksoy, S. Coskun, S. Kucukyildiz, H. E. Unalan, *Nanotechnology* **2012**, *23*, 325202; b) F. X. Wang, Y. Q. Liu, H. D. Wu, Y. Xiao, G. B. Pan, *J. Mater. Chem. C* **2013**, *1*, 422; c) K. Heo, H. Lee, Y. Park, J. Park, H. J. Lim, D. Yoon, C. Lee, M. Kim, H. Cheong, J. Park, J. Jian, S. Hong, *J. Mater. Chem.* **2012**, *22*, 2173.
[9] W. Park, G. Jo, W. K. Hong, J. Yoon, M. Choe, S. Lee, Y. Ji, G. Kim, Y. H. Kahng, K. Lee, D. L. Wang, T. Lee, *Nanotechnology* **2011**, *22*, 205204.
[10] M. Y. Chen, H. Yu, S. V. Kershaw, H. H. Xu, S. C. Gupta, F. Hetsch, A. L. Rogach, N. Zhao, *Adv. Funct. Mater.* **2014**, *23*, 53.
[11] R. Novotny, P. Lostak, J. Horak, *Phys. Scr.* **1990**, *42*, 253.
[12] a) B. Gao, M. Zhao, Q. Wang, K. B. Kang, Z. G. Xu, H. L. Zhang, *New J. Chem.* **2013**, *37*, 1692; b) B. D. Mao, C. H. Chuang, J. W. Wang, C. Burda, *J. Phys. Chem. C* **2011**, *115*, 8945.
[13] R. Vadapoo, S. Krishnan, H. Yilmaz, C. Marin, *Phys. Status Solidi B* **2011**, *248*, 700.
[14] Y. Q. Liu, M. Zhang, F. X. Wang, G. B. Pan, *J. Mater. Chem. C* **2014**, *2*, 240.
[15] T. Y. Zhai, M. F. Ye, L. Li, X. S. Fang, M. Y. Liao, Y. F. Li, Y. Koide, Y. Bando, D. Golberg, *Adv. Mater.* **2010**, *22*, 4530.
[16] P. L. Wang, T. Kolodiazhnyi, J. L. Yao, Y. Mozharivskyj, *Chem. Mater.* **2013**, *25*, 699.
[17] R. Caracas, X. Gonze, *Phys. Chem. Miner.* **2005**, *32*, 295.
[18] M. G. Gong, A. Kirkeminde, Y. Xie, R. T. Lu, J. W. Liu, J. Z. Wu, S. Q. Ren, *Adv. Opt. Mater.* **2013**, *1*, 78.
[19] a) L. Li, P. C. Wu, X. S. Fang, T. Y. Zhai, L. Dai, M. Y. Liao, Y. Koide, H. Q. Wang, Y. Bando, D. Golberg, *Adv. Mater.* **2010**, *22*, 3161; b) L. F. Hu, J. Yan, M. Y. Liao, H. J. Xiang, X. G. Gong, L. D. Zhang, X. S. Fang, *Adv. Mater.* **2012**, *24*, 2305.
[20] X. S. Fang, S. L. Xiong, T. Y. Zhai, Y. Bando, M. Y. Liao, U. K. Gautam, Y. Koide, X. Zhang, Y. T. Qian, D. Golberg, *Adv. Mater.* **2009**, *21*, 5016.
[21] a) X. Fan, X. M. Meng, X. H. Zhang, M. L. Zhang, J. S. Jie, W. J. Zhang, C. S. Lee, S. T. Lee, *J. Phys. Chem. C* **2009**, *113*, 834; b) D. S. Wang, C. H. Hao, W. Zheng, Q. Peng, T. H. Wang, Z. M. Liao, D. P. Yu, Y. D. Li, *Adv. Mater.* **2008**, *20*, 2628; c) X. Xie, S. Y. Kwok, Z. Z. Lu, Y. K. Liu, Y. L. Cao, L. B. Luo, J. A. Zapien, I. Bello, C. S. Lee, S. T. Lee, W. Zhang, *Nanoscale* **2012**, *4*, 2914.
[22] C. Y. Zhang, S. Wang, L. J. Yang, Y. Liu, T. T. Xu, Z. Y. Ning, A. Zak, Z. Y. Zhang, R. Tenne, Q. Chen, *Appl. Phys. Lett.* **2012**, *100*, 243101.
[23] J. J. Cha, J. R. Williams, D. Kong, S. Meister, H. Peng, A. J. Bestwick, P. Gallagher, D. Goldhaber-Gordon, Y. Cui, *Nano Lett.* **2010**, *10*, 1076.
[24] a) G. D. Li, D. Liang, R. L. J. Qiu, X. P. A. Gao, *Appl. Phys. Lett.* **2013**, *102*, 043104; b) E. K. Shokr, E. M. M. Ibrahim, A. M. A. Hakeem, A. M. Adam, *J. Exp. Theor. Phys.* **2013**, *116*, 166; c) Z. Ren, A. A. Taskin, S. Sasaki, K. Segawa, Y. Ando, *Phys. Rev. B* **2011**, *84*, 165311.
[25] K. A. Chandrasekharan, A. G. Kunjomana, *Turk. J. Phys.* **2009**, *33*, 209.
[26] a) C. Soci, A. Zhang, B. Xiang, S. A. Dayeh, D. P. R. Aplin, J. Park, X. Y. Bao, Y. H. Lo, D. Wang, *Nano Lett.* **2007**, *7*, 1003; b) J. D. Prades, F. Hernandez-Ramirez, R. Jimenez-Diaz, M. Manzanares, T. Andreu, A. Cirera, A. Romano-Rodriguez, J. R. Morante, *Nanotechnology* **2008**, *19*, 465501.